# Photocatalytic Activity of MWCNT-Reinforced MoS$_2$ Nanosheets

Shweta[1] · Varsha Singh[2] · Vinamrita Singh[3] · Sridharbabu Yarramaneni[4] · Mohammad Ashiq[5] · Kaushal Kumar[1] · Prikshit Gautam[6] · Arun Kumar[1]

## Abstract

Two-dimensional transition metal dichalcogenides, especially MoS$_2$, are widely exploited for their proficiency owing to the optimum energy band gap required for photocatalytic mechanism. However, the electron–hole pair recombination hampers the photocatalytic efficiency of pristine 2D MoS$_2$. In this work, multi-walled carbon nanotubes (MWCNTs) are reinforced into 2D MoS$_2$ nanosheets via an ultrasound-driven liquid exfoliation technique to synthesize an efficient photocatalyst. The resulting composite nanosheets are characterized structurally by high-resolution transmission electron microscopy (HRTEM), Fourier-transform infrared spectroscopy (FTIR), and Raman spectroscopy. The ultraviolet–visible (UV–vis) absorption and photoluminescence spectroscopy reveal changes in the band gap and the recombination rate probability of the photogenerated charge carriers, respectively. The photocatalytic performance of the composite nanosheets is investigated by photodegradation of methylene blue dye. The efficiency of the photocatalysts is studied for varying concentrations of the reinforcement. The values of rate constant (at 665 nm) are 0.0047 min$^{-1}$ for pristine MoS$_2$ nanosheets, 0.0171 min$^{-1}$, 0.0177 min$^{-1}$, and 0.0183 min$^{-1}$ for MoS$_2$@MWCNT composite nanosheets of 2%, 4%, and 8% of MWCNT, respectively. The degradation percentage is 60%, 84%, 85%, and 86% for pristine MoS$_2$, MoS$_2$@MWCNT composite nanosheets of 2%, 4%, and 8% of MWCNT, respectively. The results of the study show the enhanced degradation efficiency of the MoS$_2$@ MWCNT composite nanosheets in comparison to pristine MoS$_2$ nanosheets. Consequently, this work suggests an alternate hybrid of MoS$_2$ with MWCNTs synthesized via a rapid, easy, cost-effective, and efficient route for superior degradation efficiency, which can be beneficial for engineering hybrid structures of MoS$_2$ -based photocatalysts with promising potential for photocatalytic activities.

**Keywords** 2D MoS$_2$ · MWCNTs · composite nanosheets · photocatalysis · methylene blue dye

✉ Vinamrita Singh
vinamrita.singh@nsut.ac.in

✉ Arun Kumar
arunkumar@jcboseust.ac.in

1   Department of Physics, J.C. Bose University of Science and Technology YMCA, Faridabad, Haryana 121006, India

2   Centre for Life Sciences, Chitkara School of Health Sciences, Chitkara University, Rajpura, Punjab 140401, India

3   Department of Physics, Netaji Subhas University of Technology, East Campus, Delhi 110031, India

4   Center for Advanced Material Devices, BML Munjal University, Gurugram 122413, India

5   CSIR-Advanced Materials and Processes Research Institute (AMPRI), Hoshangabad Road, Bhopal 462026, India

6   Department of Physics, Kirori Mal College, University of Delhi, Delhi 110007, India

## Introduction

Water pollution caused by industrial effluents that contain harmful synthetic chemical dyes is a significant, global environmental problem.[1] Decomposing the hazardous components in wastewater is a key concern of the present time since the dyes pose a threat to human health. It is obvious that proper treatment of these contaminants is crucial for both the environment and public health, given the potentially harmful impacts of such contaminations. Researchers have developed an interest in solar-driven semiconductor photocatalysts because the annual irradiation of $1.5 \times 10^{18}$ kWh from the sun is over 28,000 times greater than the annual world energy consumption.[2] The growing class of two-dimensional materials, specifically transition metal dichalcogenides (TMDs), has improved photocatalytic, photovoltaic,

and optoelectronic capabilities. TMD materials are composed of layers of covalently bound atoms which are weakly stacked by van der Waals forces. They have the potential for novel scientific functionalities owing to the change in their properties as a result of the transition from their 3D to 2D form.[1,3,4] Among TMDs, molybdenum disulfide ($MoS_2$) is a typical representative of 2D material that shows promising photocatalytic behavior with favorable visible light response. Due to quantum confinement effects, 2D $MoS_2$ exhibits promising properties like high charge mobility, low power dissipation, strong photoluminescence, etc.[5]. Moreover, the thickness-dependent tuneable optical band gap switches from indirect (~1.2 eV) to direct (~1.9–2.3 eV) and hence offers good optical response in ultraviolet–visible (UV-vis) range.[6,7] Since ideal solar sensitizer catalysts must absorb a broad spectrum of radiation, including another photocatalyst with $MoS_2$ , the aim of expanding the absorption range is reasonable for more efficient elimination of organic pollutants from water. Maksoud et al.[8] reviewed the nanocomposites of $MoS_2$ for different synthesis techniques, structures, and their viable applications in the field of water treatment and energy storage.

Among the various widely studied materials, carbon nanotubes (CNTs) are another class of material with many captivating properties and applications both in their pristine form and in composite forms, especially with $MoS_2$. In 1991, the evolution of CNTs opened the pathways to innovative nanoscale technologies. CNTs are made up of carbon atoms tubular in shape with diameters in the nanorange and length up to microns, resulting in large aspect ratios.[9] MWCNTs have been widely studied because of their interesting physical, electrical, optical, and chemical properties owing to their hollow one-dimensional structure.[9,10] The interesting properties of CNTs are high tensile strength, low density or light weight, high conductivity, high thermal conductivity, high chemical and thermal stability, special electronic structures, and high elasticity.[9] CNTs are exploited in many research areas including materials science, electronics, optics, nanotechnology, and nanomedicine. The reported applications of CNTs include transistors, biosensors, vacuum electronic devices, capacitors, membranes, drug delivery, water treatment, etc.[9,10]. In recent times, Zhang et al.[11] reviewed in detail the applications of CNT-based materials for photocatalysis. Another possible and seldom researched nanocomposite in the field of optoelectronics combines MWCNTs with $MoS_2$.

A few of the available studies in the literature regarding the nanocomposites of $MoS_2$ and CNTs are based on the energy harvesting properties of the combined material. $MoS_2$/CNT hybrids may prove to be better catalysts for hydrogen evolution reactions (HER) and other practical supercapacitor applications. It is reported in the literature that incorporating CNTs in the exfoliation process of $MoS_2$ helps in better exfoliation by reducing the chances of restacking of nanosheets along with improved electrochemical applications.[12] Cao et al.[13] synthesized $MoS_2$ nanosheets on MWCNTs using a hydrothermal method and the heterostructures imparted enhanced HER performance. In another work, 2D $MoS_2$ sheets are rolled over carbon nanotubes to form tubular structures for lithium storage applications.[14,15] This is proposed as a multifunctional heterostructure for energy storage and energy conversion devices. Dastborhan et al.[16] introduced a flower-like nanocomposite of $MoS_2$ and CNTs and identified the proficient sonocatalytic properties by showing the degradation of hydroxychloroquine (HCQ). Liu et al.[15] demonstrated the use of liquid-phase exfoliated $MoS_2$ nanosheets reinforced with single-walled CNTs for sodium ion batteries. The composite material was reported to be low-cost, highly mechanically stable, and a high-capacity electrode material with high volumetric/areal loading. Yan et al.[17] reported the potential of a Co-$MoS_2$/CNT catalytic membrane for wastewater treatment which degraded RhB dye up to 80% within 1 h. In another work, CNTs/ZnO/$MoS_2$ nanocomposites were reported to exhibit considerable photocatalytic efficiency in degradation of aniline in aqueous solution under visible light illumination.[18] Furthermore, there are some reports of the application of $MoS_2$–carbon material composites for their optical and photocatalytic applications, especially for water remediation. For instance, Zou et al.[19] presented a $MoS_2$/rGO composite material for the successful degradation of ranitidine under the illumination of visible light. In another work, a unique photocatalyst of $MoS_2$ and rGO, coated with red phosphorous, was synthesized to study the photodegradation of chromium (98.0%) and Rhodamine B (99.3%) within 30 min.[20] Gusain et al.[21] presented a $MoS_2$/MWCNT nanocomposite photocatalyst for the removal of cadmium and lead from industrial water. Liang et al.[22] reported a composite of $MoS_2$ with carbon nanofibers as a commendable photocatalyst, synthesized via electrospinning. In the literature, there are a few other studies regarding composites of $MoS_2$ with graphitic carbon nitride for photocatalytic water remediation, which show the promising potential of the composites in the field of photocatalysis.[23–26] Thus, $MoS_2$ and CNT composites are viable options for improved photocatalytic applications.

Notably, regarding the photocatalytic dye degradation performance, changes in the $MoS_2$ response on reinforcing with MWCNTs have not been widely explored. In addition, to our best knowledge, liquid-phase exfoliated 2D $MoS_2$@MWCNTs nanocomposites for photocatalytic performance of methylene blue (MB) dye are not found in literature. In this context, pristine $MoS_2$ nanosheets and MWCNT-reinforced $MoS_2$ nanosheets have been synthesized using ultrasound-driven liquid exfoliation for comparatively

studying the degradation of MB dye. The effect of varying the MWCNT concentration on the dye degradation has been analyzed to optimize the composition.

## Experimental

### Materials

Bulk MoS$_2$ powder (atomic particle size 60–70 $\mu$m and purity 99.9%) and multi-walled carbon nanotubes (Ø: 10–20 nm, length: 3–8 $\mu$m and purity 99%) were purchased from Nanoshel. Solvent N-methylpyrrolidone (NMP) with purity 99% of analytical grade was purchased from CDH.

### Synthesis of MoS$_2$@MWCNTs Nanosheets

The MoS$_2$ powder was ground in an agate mortar pestle for 4 h. While grinding, 0.1 mL NMP was added after every 1 h to balance the evaporated solvent. The powder was then dried in an oven at 60°C before being divided into four equal batches: one for pristine MoS$_2$ nanosheets and three in which MWCNTs were added to the powder in varying concentrations of 2%, 4%, and 8%. These were then stirred magnetically at 1000 rpm for 24 h in NMP solvent (with a concentration of 50 mg/mL). Thereafter, probe sonication (LABSONIC Probe Sonicator, 1200 W) was used for mechanical exfoliation of the samples. This process is

carried out at 5°C for 2 h with an on/off cycle of 8/2 s. The sonicated solutions were allowed to sediment naturally after which the lighter exfoliated nanosheets were separated by a centrifuge (5000 rpm for 30 min). The 2/3$^{rd}$ portions of the supernatant of all the samples were decanted, resulting in four samples with the details and coding shown in Table I. The synthesis procedure of the nanosheets is shown in Fig. 1.

### Photocatalytic Degradation Experiment

The photocatalytic degradation of MB was examined under the exposure of UV and visible light lamps each of 300 W. An amount of 10 ppm of MB dye solution was divided equally into four solutions of 40 mL each. Next, 20 mg of MoS$_2$ and MoS$_2$@MWCNT (2 M/C, 4 M/C, and 8 M/C) photocatalysts were added to the four separate dye solutions, which were then magnetically stirred for 30 min at 500 rpm under dark conditions to attain adsorption/desorption equilibrium. Thereafter, the resultant samples were exposed to UV-vis light and the dye degradation response was investigated by measuring the absorption spectrum of 3-mL solutions collected every 30 min up to 120 min.

### Characterizations

The absorption spectra of the samples were measured using a Shimadzu UV-3600i plus UV-VIS-NIR Spectrophotometer to investigate the optical and photocatalytic properties of the exfoliated nanosheets. Raman studies and photoluminescence emission spectra of the suspensions were acquired using WITec – ALPHA300 RAS Microscope with a 355-nm laser source after drying the samples on a glass slide. Fourier-transform infrared (FTIR) spectroscopy data were recorded from 400 cm$^{-1}$ to 4000 cm$^{-1}$ for structural analysis using a Perkin-Elmer Spectrum Two FTIR spectrometer. High-resolution transmission electron microscopy (HR-TEM; JEM-F200; JEOL) with selected area electron diffraction (SAED) was used for the morphological studies. For HRTEM, ~ 1 mg of dried nanocomposites were

**Table I** Coding of samples with details (2/4/8 refers to weight percentages of MWCNTs in MoS$_2$ and M/C designates the composite)

| Concentration of MWC-NTs (wt%) | Sample coding | Band gap (eV) |
|---|---|---|
| 0 | Bulk MoS$_2$ | 1.4 |
| 0 | Exfoliated MoS$_2$ | 2.16 |
| 2 | 2 M/C | 2.8 |
| 4 | 4 M/C | 2.5 |
| 8 | 8 M/C | 2.7 |

Band gap of samples calculated by extrapolation of Tauc plots



**Fig. 1** Synthesis process of pristine MoS$_2$ and MoS$_2$@MWCNT composite nanosheets.

sonicated in 1 mL isopropanol for 60 s and drop-cast on a 300-mesh carbon-coated copper grid.

## Results and Discussion

### Structural Analysis

FTIR spectra analysis gives information of the structure in terms of existing functional groups. It is employed to confirm the coexistence of $MoS_2$ and MWCNTs in the prepared samples along with structural deformations, if any. Figure 2a shows the Mo-S stretching vibration located at $467 \ cm^{-1}$, and the C=C stretching mode and ordered phase of MWCNTs at $1540 \ cm^{-1}$ and around $1600–1650 \ cm^{-1}$, respectively.[27,28] In addition, another broad $1400–1675 \ cm^{-1}$ band corresponds to the O-H bending vibrations, while the band from $3000 \ cm^{-1}$ to $3500 \ cm^{-1}$ may account for H-O-H stretching vibrations.[29,30] It is clear that the synthesized samples have both $MoS_2$ and MWCNTs successfully incorporated, resulting in heterostructures. Moreover, the same FTIR peaks for all the composite samples imply that the weight percentage of the reinforcement does not create any structural differences or deformations in the samples.

Raman spectra analysis was employed for additional confirmation of the formation of $MoS_2$@MWCNTs heterostructures. Figure 2b depicts the positions of two characteristic Raman peaks of $MoS_2$, namely $E_{2g}^1$ and $A_g^1$, at $384.48 \ cm^{-1}$ and $405.65 \ cm^{-1}$, respectively. The two peaks correspond to in-plane and out-of-plane vibrations of sulfur atoms, respectively, and the frequency difference between them was $21.17 \ cm^{-1}$. In the composite samples, broad CNT D, G, and G' bands are seen around $1300 \ cm^{-1}$, $1800 \ cm^{-1}$, and $2500 \ cm^{-1}$, respectively. The D band refers to the defects and disordering in the CNTs, the G band refers to in-plane $E_{2g}$ stretching of $sp^2$ carbon atoms, and G' is the overtone of the D band.[31–33] The minor downshift in the G band arises from the electronic interaction between the MWCNTs and $MoS_2$.[34] The nanotube reinforcement is equivalent to randomly oriented fiber-reinforced formation of the composites. The synergistic effects of random orientations and the high-intensity ultrasonication process address the broadening of the Raman peaks, and the resulting stress-induced peak shifts towards a lower wavenumber (shown by dotted lines in Fig. 2b).[35] The broad peak at ~ $500 \ cm^{-1}$ indicates the presence of amorphous carbon, which may have resulted from the high-intensity probe sonication of the samples. It is observed that, in the composite nanosheets, the $MoS_2$ peaks are not clearly visible, which may be attributed to the low dispersion of MWCNT-mediated $MoS_2$, resulting in a lower yield of nanosheets obtained after the centrifuge process. In other words, it can be suggested that the MWCNTs outshine $MoS_2$. Moreover, the concentration effects of the MWCNTs seem to be ineffective for Raman modes.

### Optical Properties

Figure 3a and b showing the PL spectra of all the samples reflect the following points: (1) two emission peaks at 460 nm and 540 nm for pristine $MoS_2$ nanosheets are associated with the transition from an indirect to a direct band gap and confirm the few-layers range of $MoS_2$,[36] (2) high-intensity PL emission peaks at 450 nm and 510 nm for pure MWCNTs, (3) PL emission peaks of $MoS_2$@MWCNTs nanosheets around 458 nm and 535 nm indicate the direct band gap in 2D composite nanosheets, and (4) with the increase in the MWCNT content in $MoS_2$, an increase in the intensity of the PL peaks is observed and is at a minimum for the 2% reinforcement case. The PL peaks
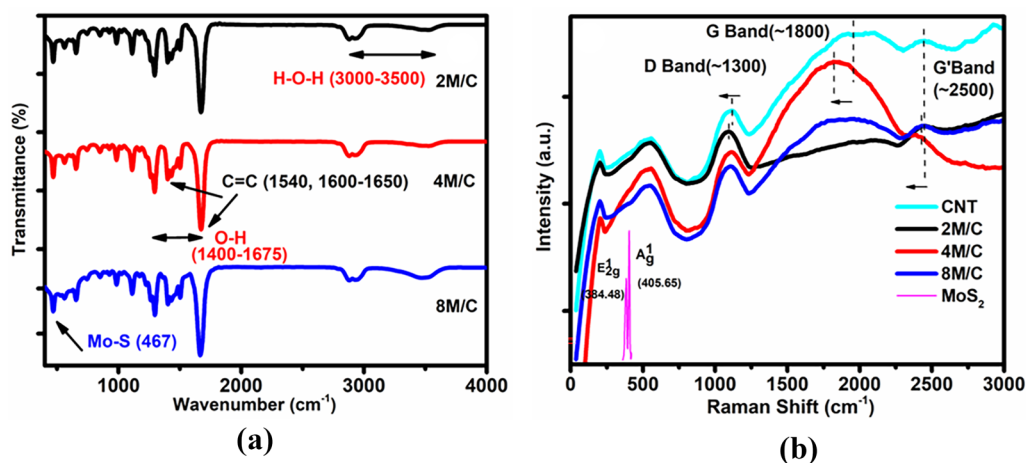


**Fig. 2** (a) FTIR spectra of $MoS_2$@MWCNTs nanosheets and (b) Raman spectra of pristine $MoS_2$ and of $MoS_2$@MWCNTs nanosheets.
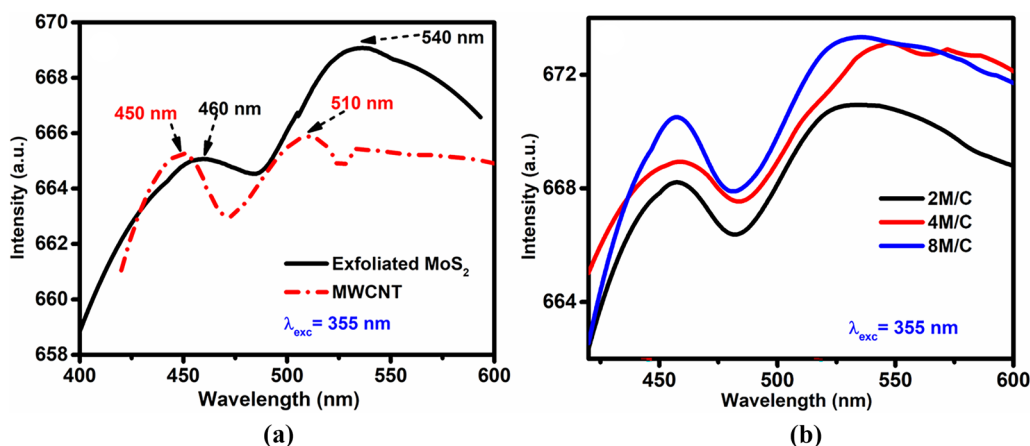
**Fig. 3** PL spectra of (a) exfoliated MoS$_2$ and MWCNTs and (b) MoS$_2$@MWCNTs nanosheets.

normally imply the recombination of electron–hole pairs, band to band or band to defect charge transfer. Here, the increase in peak intensity with addition of MWCNTs may be attributed to the additional charge pathways generated in the composite. In the case of MoS$_2$ and MWCNTs, the charge transfer occurs from MWCNTs to MoS$_2$ with the transferred electrons residing on the sulfur atoms.[34]
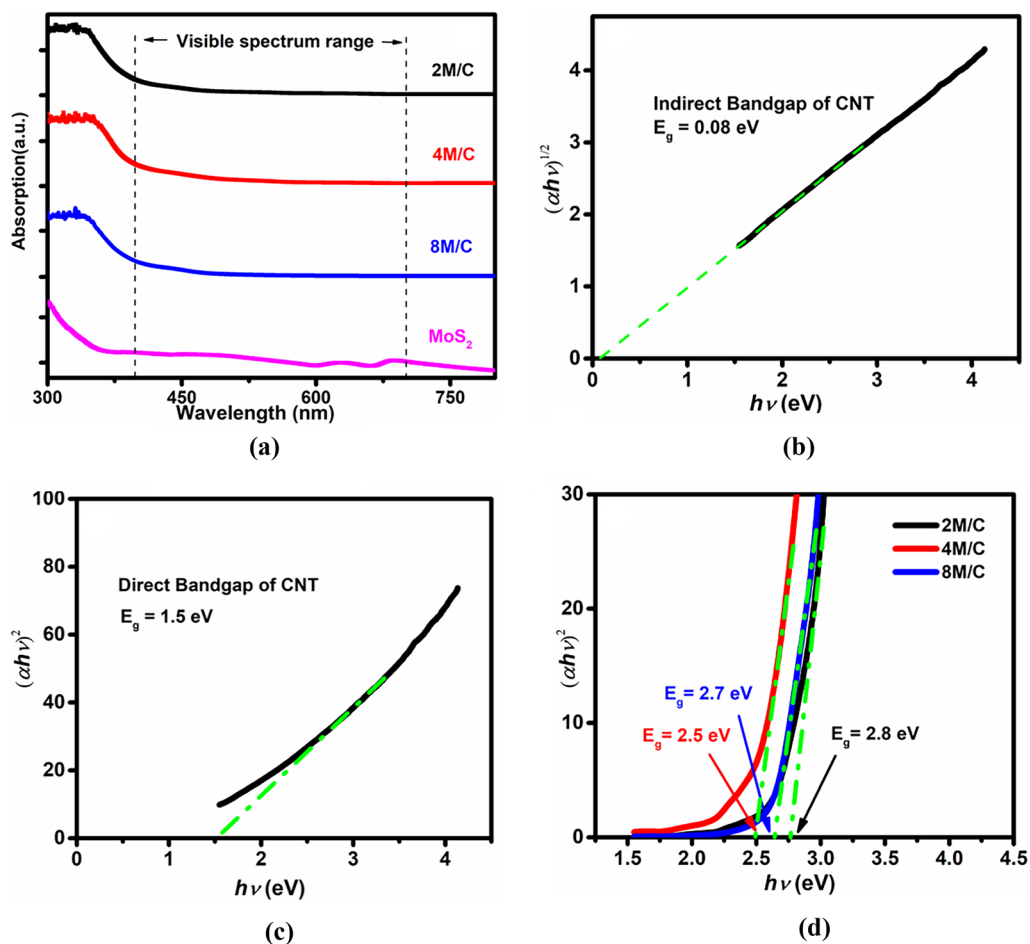


**Fig. 4** (a) Absorption spectra of pristine MoS$_2$ nanosheets and MoS$_2$@MWCNTs nanosheets. Tauc plots of pristine MWCNTs (b) for indirect band gap, (c) direct band gap, and (d) MoS$_2$@MWCNTs nanosheets.
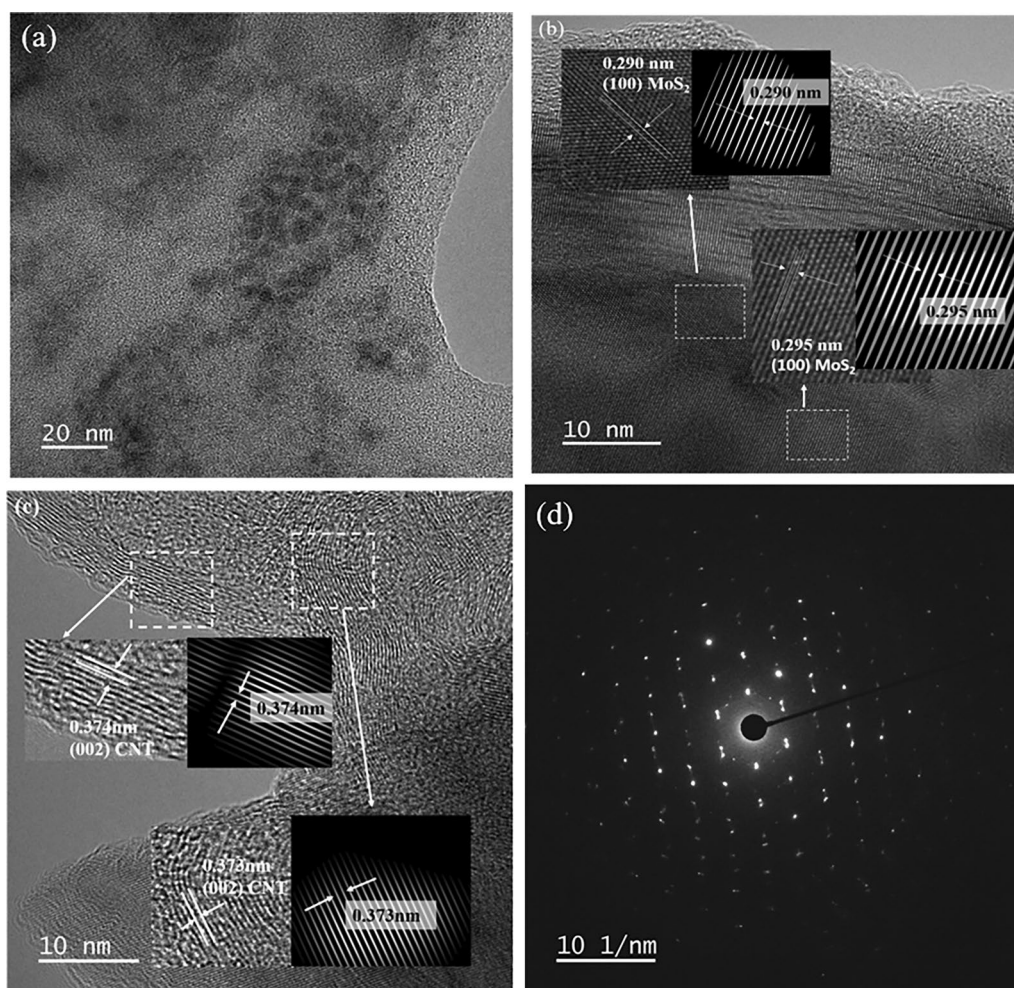
**Fig. 5** (a–c) HRTEM images and (d) SAED pattern of $MoS_2$/MWCNTs nanosheets.

UV-vis absorption peaks give insight into the range of absorption and the band gaps of $MoS_2$, MWCNTs, and the composite. Figure 4a shows that pristine 2D $MoS_2$ nanosheets exhibit four absorption peaks at A ~ 669 nm, B ~ 604 nm, C ~ 442 nm, and D ~ 401 nm. Peaks A and B correspond to the smallest direct transition of electrons from the top of valence band (VB) to the bottom of the conduction band (CB), and peaks C and D correspond to direct transitions occurring from deep VB to CB.[37,38] Also, it can be seen from the graph that the composite nanosheets show more absorbance in the UV range (characteristic of MWCNTs), while no 2D $MoS_2$ characteristic absorption peaks are observed, and with no effect of the concentration, which may again be due to low dispersion of the $MoS_2$ in the composites, as mentioned above.

For further continual optimization, band gap values ($E_g$) were computed for the prepared samples using Tauc's relationship $\left[ (\alpha h\upsilon)^{\frac{1}{n}} = C\left(h\upsilon - E_g\right) \right]$, where $h\upsilon$ is the incident radiation energy, $C$ is the proportionality constant, $n$ is either ½ or 2 for direct and indirect band gaps, respectively, and $\alpha$ is the absorption coefficient which is calculated from $\alpha = 2.303 \log\left(\frac{A}{d}\right)$, where $A$ is the absorbance and $d$ is the path length.[39] Figure 4b, c, and d shows the respective computed values of the indirect band gap of pure MWCNTs ~ 0.08 eV, the direct band gap of pure MWCNTs ~ 1.5 eV, and the direct band gap of the synthesized composite samples that are also mentioned in Table I. The obtained values of the band gaps agree with the literature.[40–44]

## Morphological Analysis

To confirm the coexistence of MWCNTs and 2D $MoS_2$ layers in the resulting composite nanosheets and their morphologies, HRTEM images and SAED patterns at different magnifications and at different regions of the samples are shown in Fig. 5a, b, c, and d. A few dispersed $MoS_2$ with
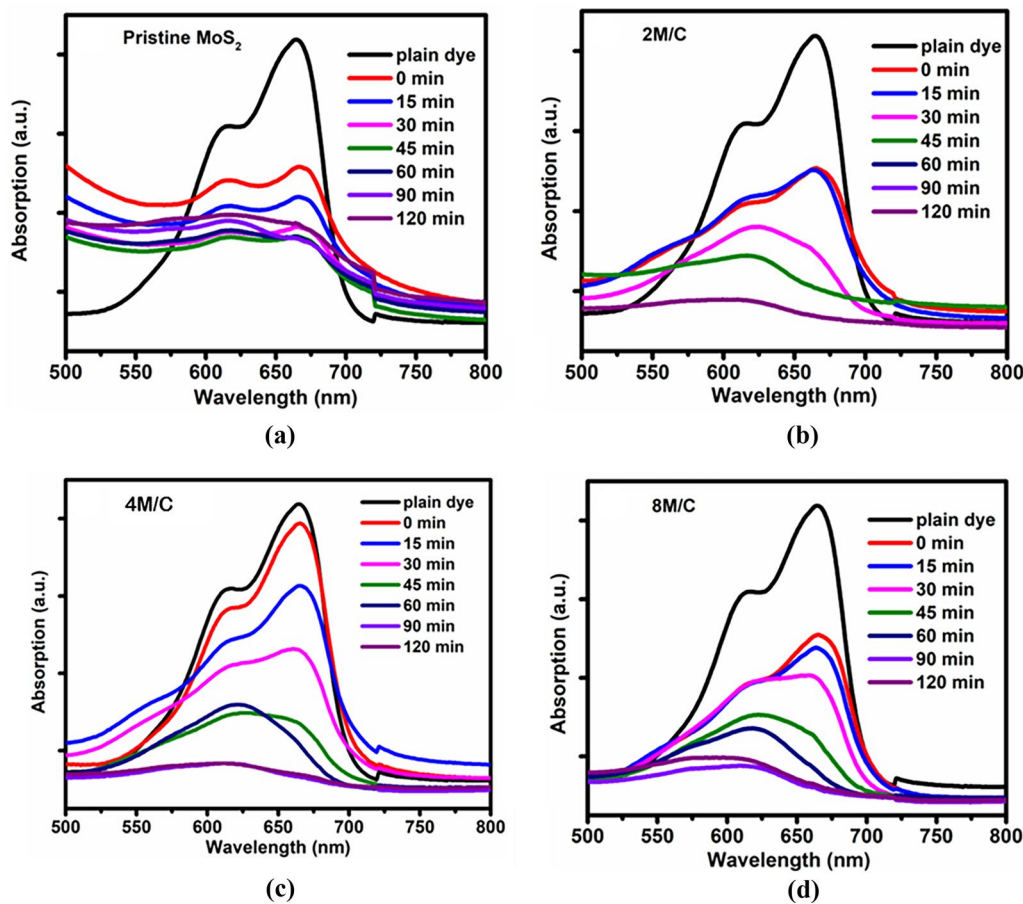
**Fig. 6** UV–vis absorption spectra of (a) pristine MoS$_2$, (b) 2 M/C, (c) 4 M/C, and (d) 8 M/C nanosheets for 120 min.

MWCNTs resulting in particle-like morphology can be seen in Fig. 5a.

The crystal lattice fringes of the MWCNTs (0.374 nm corresponding to the (002) plane) and MoS$_2$ (0.29 nm can be indexed to the (100) plane) are shown in Fig. 5b and cm, respectively. In addition, the SAED pattern (Fig. 5d) displays the hexagonal symmetry of MoS$_2$ incorporated with crystalline MWCNTs.

## Photocatalytic Dye Degradation Analysis

The degradation of MB under UV-vis light is examined for the four different samples: (1) pristine MoS$_2$ nanosheets, (2) 2 M/C, (3) 4 M/C, and (4) 8 M/C composite nanosheets. Figure 6a, b, c, and d shows the UV-vis spectra of the samples from 0 min to 120 min of exposure. The absorption peaks of MB appear at 665 nm (monomer) and 617 nm (dimer). After 120 min of exposure to UV-vis light, there is a reduction in absorption peaks in the presence of the photocatalysts, indicating degradation of MB. The decrease in peak intensity is

the minimum for pristine MoS$_2$ and the maximum for the MoS$_2$@MWCNT samples.

The progress of degradation has been estimated by studying the kinetics of dye degradation which follows a pseudo-first-order model, given by Eq. (1). The dye degradation percentage is calculated by using Eq. (2) [45]:

$$\ln\left(\frac{C_t}{C_0}\right) = -kt \tag{1}$$

$$D(\%) = \frac{C_0 - c_t}{C_0} \times 100 \tag{2}$$

where $C_0$ and $C_t$ are the dye concentrations at times 0 s and $t$ s, respectively, and $k$ is the rate constant.

Figure 7a shows the percentage of photodegradation based on the two characteristic peaks of MB for the samples, which are 86% (8 M/C) > 85% (4 M/C) > 84% (2 M/C) > 60% (MoS$_2$). This shows that the samples have good efficiency and potential for photodegradation with maximum efficacy for MoS$_2$@MWCNT in comparison to the pristine MoS$_2$ nanosheets. Furthermore, the
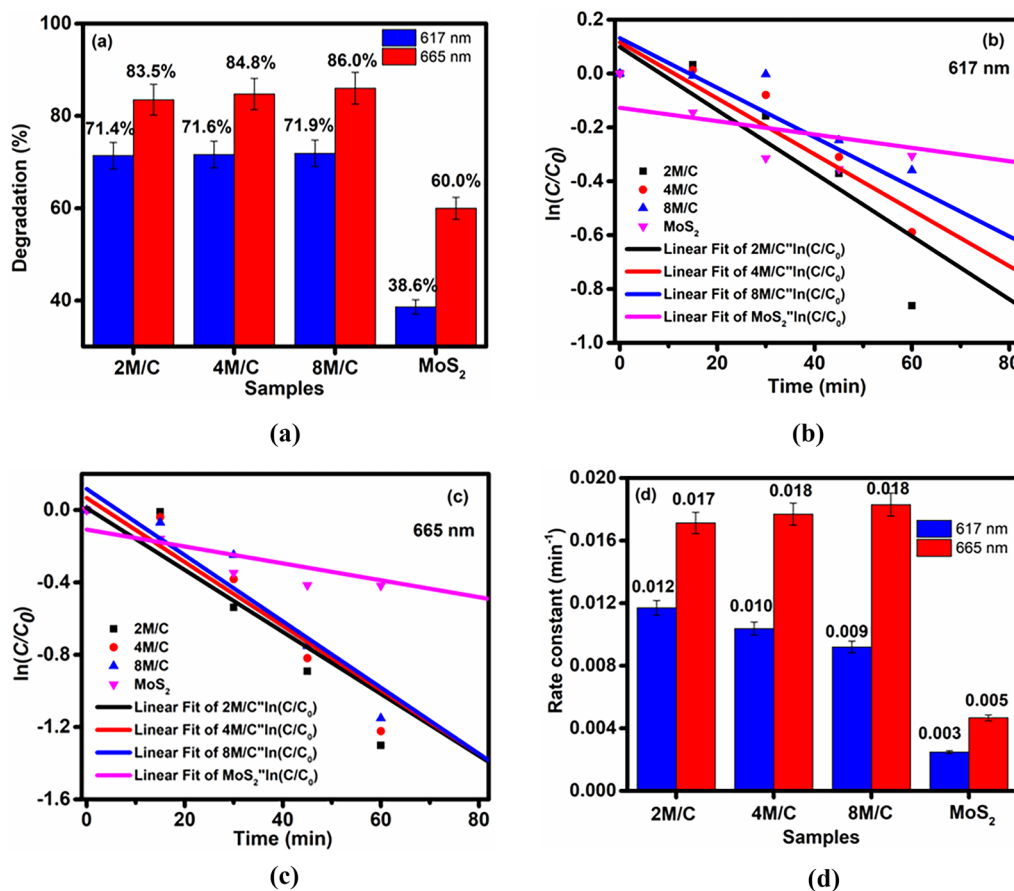
**Fig. 7** (a) Degradation percentages (with 4% error bars), (b) linear fits of ln ($C/C_0$) versus time at 617 nm, (c) linear fits of ln ($C/C_0$) versus time at 665 nm, and (d) rate constant values (with 4% error bars) of pristine $MoS_2$ and $MoS_2$@MWCNTs nanosheets.

degradation mechanism can occur under both dark and light illumination. The degradation under dark conditions is attributed to the adsorption of dye molecules on the surface of the photocatalysts. For the light illumination, the degradation occurs via redox reactions between the photogenerated charges and the organic dye.[46] The degradation percentages at 0 min correspond to the dark condition degradation mechanism of 38% for $MoS_2$ and 39% for the $MoS_2$@MWCNT composite nanosheets. Figure 7b (at 617 nm) and (c) (at 665 nm) shows the ln ($C_t/C_0$) as a function of time. In addition, the first-order rate constant is computed from the slope of the ln ($C_t/C_0$) versus time graph (shown in Fig. 7d). The values of the rate constant (at 665 nm) are 0.0047 $min^{-1}$ for pristine $MoS_2$ nanosheets, 0.0171 $min^{-1}$, 0.0177 $min^{-1}$, and 0.0183 $min^{-1}$ for 2 M/C, 4 M/C, and 8 M/C, respectively. These results indicate the enhanced photocatalytic degradation of MB dye due to $MoS_2$@MWCNT composite nanosheets compared to pristine $MoS_2$ nanosheets. Furthermore, with the increase in mass loading of MWCNTs in $MoS_2$, the rate constant and degradation percentage increase. A brief outline of the review of carbon-based
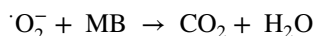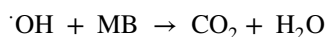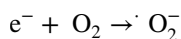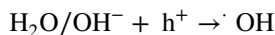
heterostructures of $MoS_2$ for photocatalytic applications in terms of the synthesis route and the resulting properties is shown in Table II.

$MoS_2$ and MWCNTs act as photosensitizers utilizing a wider spectrum of incident light along with improved charge separation compared to lone material. Under light irradiation, electron–hole pair generation occurs by absorbing photons of sufficient energy. For pristine $MoS_2$ nanosheets, the electrons and holes recombine readily compared to the $MoS_2$@ MWCNT composite due to the lack of a suitable junction. Efficient photocatalysis essentially requires the formation of a junction between two semiconductors at which the dissociation of electron–hole pairs can occur. In composite photocatalysts, the synergistic influence between $MoS_2$ and the MWCNTs leads to the formation of heterogeneous interfaces and additional reactive sites, thus causing improved photocatalytic potential. In the case of $MoS_2$@MWCNT, the photoinduced electrons in the MWCNTs are injected into the CB of $MoS_2$ triggering the redox reactions. Simultaneously, the light absorbed by the $MoS_2$ also leads to the creation of electron–hole pairs, and it is very plausible that electrons injected from the VB of $MoS_2$ to the MWCNTs generate additional

**Table II** A review of carbon-based heterostructures of MoS$_2$ for photocatalytic applications from literature

| Sample | Photocatalytic material | Methods | Inferences | Ref. |
|---|---|---|---|---|
| 1 | MoS$_2$/rGO composite synthesized by a hydrothermal route | Investigated for photocatalytic degradation of ranitidine | Impressive performance with 74% ranitidine photodegraded in 60 min under visible light | 19 |
| 2 | Red phosphorous-MoS$_2$/rGO photocatalyst fabricated via a hydrothermal route | Synergy removal of chromium and Rhodamine B | Photodegradation of chromium (98.0%) and Rhodamine B (99.3%) within 30 min | 20 |
| 3 | MoS$_2$/carbon nanofiber foxtail-like composites designed by electrospinning and a solvothermal method | Investigated for photocatalytic degradation of Methyl orange, MB, and Rhodamine B | After visible-light irradiation of 150 min, the degradation percentages of Methyl orange, MB, and Rhodamine B were 79.6%, 73.5%, and 62.4%, respectively | 22 |
| 4 | MoS$_2$/graphitic carbon nitride photocatalyst fabricated via ultrasonic dispersion and annealing | Demonstrated for bisphenol A (BPA) degradation | Achieved a superior photoefficiency towards BPA degradation | 23 |
| 5 | MoS$_2$ quantum dots/graphitic carbon nitride heterojunction composite prepared by polymerization | Investigated for visible-light-driven photocatalytic performance toward the photodegradation of organic pollutants | Degradation for Methyl orange: 40 min/96.3%, and for phenol: 100 min/74.8%, under visible light illumination | 25 |
| 6 | Co-MoS$_2$/CNT membrane synthesized by a photothermal method | Investigated for wastewater treatment | Degradation of Rhodamine B reached up to 80 % within 1 h | 17 |
| 7 | Synthesis of the flower-like MoS$_2$/CNTs nanocomposite via a hydrothermal route | Sonocatalytic degradation of hydroxychloroquine | 70% of HCQ degraded using 0.1 g/L of MoS$_2$/CNTs (10:1) nanocomposite within 120 min of sonocatalysis. | 16 |
| 8 | MoS$_2$@MWCNT composite nanosheets via ultrasound-driven liquid exfoliation | Investigated for photodegradation of MB | Degradation of MB reached up to 86% within 120 min of illumination of UV-vis light | This work |

holes.[47] This interfacial charge transfer between $MoS_2$ and MWCNTs hinders the electron–hole recombination process across the interface.[47–49] The accumulated resulting holes in $MoS_2$ react with water molecules ($H_2O$) or hydroxyl ions ($OH^-$), producing hydroxyl radicals ($^\bullet OH$), and the electrons react with oxygen ($O_2$) to produce superoxide radicals ($^\bullet O_2^-$). These radicals undergo chemical reactions with MB, decomposing it into nonharmful compounds - $CO_2$ and $H_2O$.[50]

$$H_2O/OH^- + h^+ \rightarrow {}^\bullet OH$$

$$e^- + O_2 \rightarrow {}^\bullet O_2^-$$

$${}^\bullet OH + MB \rightarrow CO_2 + H_2O$$

$${}^\bullet O_2^- + MB \rightarrow CO_2 + H_2O$$

## Conclusions

2D $MoS_2$@MWCNTs nanosheets have been successfully prepared via a two-step, sequential liquid exfoliation process. On investigating the structural characterization results of the prepared samples, coexistence of $MoS_2$ and MWCNTs in the composite nanosheets with no structural deformations can be inferred from FTIR and Raman spectra. Next, PL spectra indicate the increase in the recombination rate of photogenerated electron–hole pairs with the increase in the quantity of MWCNT reinforcements in $MoS_2$. In addition, low dispersion of MWCNT-mediated $MoS_2$ resulting into a lower yield of nanosheets can be observed from UV–vis, Raman, HRTEM images, lattice fringe values, and SAED patterns. The photocatalytic results indicate better light absorption, efficient electron–hole pair generation, and improved charge separation, leading to superior photocatalytic performance in the case of the $MoS_2$@MWCNT nanocomposites. Moreover, it is observed that, with the increase in mass loading of MWCNTs in $MoS_2$, the rate constant and degradation percentage increase.

Hence, it can be concluded that optimum-quality $MoS_2$@MWCNTs composite nanosheets in a few-layer range have the potential to exhibit enhanced properties in comparison to pristine $MoS_2$ nanosheets. This study may provide further possible manipulations in the development of composite nanosheets of $MoS_2$ that can be extended to other materials besides MWCNTs for effective photocatalytic applications.

## References

1. K. Dharamalingam, B. Arjun Kumar, G. Ramalingam, S. Sasi Florence, K. Raju, P. Senthil Kumar, S. Govindaraju, and E. Thangavel, *Chemosphere* 294, 133725 (2022).
2. M. Sabarinathan, S. Harish, J. Archana, M. Navaneethan, H. Ikeda, and Y. Hayakawa, *RSC Adv.* 7, 24754 (2017).
3. P.J. Ko, A. Abderrahmane, T.V. Thu, D. Ortega, T. Takamura, and A. Sandhu, *J. Nanosci. Nanotechnol.* 15, 6843 (2015).
4. M. Timpel, G. Ligorio, A. Ghiami, L. Gavioli, E. Cavaliere, A. Chiappini, F. Rossi, L. Pasquali, F. Gärisch, E.J.W. List-Kratochvil, P. Nozar, A. Quaranta, R. Verucchi, and M.V. Nardi, *NPJ 2D Mater. Appl.* 2021(5), 1 (2021).
5. V. Singh, K. Kumar, and A. Kumar, *Model Simul. Mat. Sci. Eng.* 32, 035005 (2024).
6. D. Gupta, V. Chauhan, and R. Kumar, *Inorg. Chem. Commun.* 121, 108200 (2020).
7. M.V. Olenchuk, U.K. Afonina, O.P. Gnatyuk, V.V. Strelchuk, A.S. Nikolenko, and G.I. Dovbeshko, *Mol. Cryst. Liquid Cryst.* (2022). https://doi.org/10.1080/15421406.2022.2067669.
8. M.I.A. Abdel Maksoud, A.G. Bedir, M. Bekhit, M.M. Abouelela, R.A. Fahim, A.S. Awed, S.Y. Attia, S.M. Kassem, M.A. Elkodous, G.S. El-Sayyad, S.G. Mohamed, A.I. Osman, A.H. Al-Muhtaseb, and D.W. Rooney, *Environ. Chem. Lett.* 2021(19), 3645 (2021).
9. S. Rathinavel, K. Priyadharshini, and D. Panda, *Mater. Sci. Eng. B Solid State Mater. Adv. Technol.* 268, 106996 (2021).
10. N. Anzar, R. Hasan, M. Tyagi, N. Yadav, and J. Narang, *Sens. Int.* 1, 100003 (2020).
11. J. Zhang, M. Dai, S. Zhang, M. Dai, P. Zhang, S. Wang, and Z. He, *Solar RRL* 6, 2200243 (2022).
12. W. Han, Y. Xia, D. Yang, and A. Dong, *Chem. Commun.* 57, 4400 (2021).
13. J. Cao, J. Zhou, Y. Zhang, and X. Liu, *Sci. Rep.* 2017(7), 1 (2017).
14. Q. Wang, and J. Li, *J. Phys. Chem. C* 111, 1675 (2007).
15. Y. Liu, X. He, D. Hanlon, A. Harvey, J.N. Coleman, and Y. Li, *ACS Nano* 10, 8821 (2016).
16. M. Dastborhan, A. Khataee, S. Arefi-Oskoui, and Y. Yoon, *Ultrason. Sonochem.* 87, 106058 (2022).
17. Z. Yan, X. Chen, S. Bao, H. Chang, H. Liu, G. Fan, Q. Wang, X. Fu, F. Qu, and H. Liang, *Sep. Purif. Technol.* 303, 122207 (2022).
18. P. Ghasemipour, M. Fattahi, B. Rasekh, and F. Yazdian, *Sci. Rep.* 10, 4414 (2020).
19. X. Zou, J. Zhang, X. Zhao, and Z. Zhang, *Chem. Eng. J.* 383, 123084 (2020).
20. X. Bai, Y. Du, X. Hu, Y. He, C. He, E. Liu, and J. Fan, *Appl. Catal. B* 239, 204 (2018).
21. R. Gusain, N. Kumar, E. Fosso-Kankeu, and S.S. Ray, *ACS Omega* 4, 13922 (2019).
22. H. Liang, J. Bai, T. Xu, and C. Li, *Vacuum* 172, 109059 (2020).
23. H. Liu, J. Liang, L. Shao, J. Du, Q. Gao, S. Fu, L. Li, M. Hu, F. Zhao, and J. Zhou, *Colloids Surf A Physicochem Eng Asp* 594, 124668 (2020).
24. K. Pramoda, U. Gupta, M. Chhetri, A. Bandyopadhyay, S.K. Pati, and C.N.R. Rao, *ACS Appl. Mater. Interfaces* 9, 10664 (2017).
25. L. Shi, Z. He, and S. Liu, *Appl. Surf. Sci.* 457, 30 (2018).

26. Y. Zhang, X. Yang, Y. Wang, P. Zhang, D. Liu, Y. Li, Z. Jin, B.B. Mamba, A.T. Kuvarega, and J. Gui, *Appl. Surf. Sci.* 518, 146191 (2020).

27. M.U.D. Naik, Y.S. Lee, and A. Qurashi, *ACS Omega* 3, 10442 (2018).

28. S.S. Kish, A. Rashidi, H.R. Aghabozorg, and L. Moradi, *Appl. Surf. Sci.* 256, 3472 (2010).

29. R. Verma, J. Gangwar, and A.K. Srivastava, *RSC Adv.* 7, 44199 (2017).

30. C. Prabukumar, M.M.J. Sadiq, D.K. Bhat, and K.U. Bhat, *AIP Conf. Proc.* 1943, 020084 (2018).

31. H. Xia, Y. Wang, J. Lin, and L. Lu, *Nanoscale Res. Lett.* 6, 595 (2011).

32. G.J.H. Melvin, Q.Q. Ni, Y. Suzuki, and T. Natsuki, *J. Mater. Sci.* 49, 5199 (2014).

33. L. Zhang, J. Yang, X. Wang, B. Zhao, and G. Zheng, *Nanoscale Res. Lett.* 9, 1 (2014).

34. V.O. Koroteev, L.G. Bulusheva, I.P. Asanov, E.V. Shlyakhova, D.V. Vyalikh, and A.V. Okotrub, *J. Phys. Chem. C* 115, 21199 (2011).

35. C.A. Cooper, R.J. Young, and M. Halsall, *Compos. Part A Appl. Sci. Manuf.* 32, 401 (2001).

36. S. Sarma, and S.C. Ray, *Appl. Surf. Sci.* 474, 227 (2019).

37. E.P. Nguyen, B.J. Carey, T. Daeneke, J.Z. Ou, K. Latham, S. Zhuiykov, and K. Kalantar-Zadeh, *Chem. Mater.* 27, 53 (2015).

38. V. Shweta, K. Singh, and S. Kumar, *ECS J. Solid State Sci. Technol.* 12, 031009 (2023).

39. N. Saha, A. Sarkar, A.B. Ghosh, A.K. Dutta, G.R. Bhadu, P. Paul, and B. Adhikary, *RSC Adv.* 5, 88848 (2015).

40. R. De Aguiar Ramos, M.H. Boratto, M.S. Li, and L.V. De Andrade Scalvi, *Mater. Res.* 20, 866 (2017).

41. S. Mutyala, M. Mohamed Jaffer Sadiq, M. Gurulakshmi, C. Suresh, D. KrishnaBhat, K. Shanthi, and J. Mathiyarasu, *J. Nanosci. Nanotechnol.* 20, 1118 (2019).

42. Journal of Advances in Physics **11**, 3546 (2016).

43. M. Saadati, O. Akhavan, and H. Fazli, *Catalysts* 11, 1445 (2021).

44. Z.Y. Zhao, and Q.L. Liu, *Catal. Sci. Technol.* 8, 1867 (2018).

45. J. Kisała, R. Wojnarowska-Nowak, and Y. Bobitski, *Sci. Rep.* 2023(13), 1 (2023).

46. F. Zhou, W. Liu, Z. Miao, and Q. Wang, *ChemistrySelect* 4, 7260 (2019).

47. W. Wang, P. Serp, P. Kalck, and J.L. Faria, *J. Mol. Catal. A Chem.* 235, 194 (2005).

48. P.V. Kamat, I. Bedja, and S. Hotchandani, *J. Phys. Chem.* 98, 9137 (1994).

49. A. Saha, A. Moya, A. Kahnt, D. Iglesias, S. Marchesan, R. Wannemacher, M. Prato, J.J. Vilatela, and D.M. Guldi, *Nanoscale* 9, 7911 (2017).

50. K. Ramsha, R. Adeel, J. Sofia, J. Rahim, A.A. Muhammad, and M. Mohammad, *Key Eng. Mater.* 778, 137 (2018).